*Manuscript
Click here to view linked References

Synchrotron Quantification of Ultrasound Cavitation and Bubble Dynamics in Al-10Cu Melts

W.W. Xu[1,2], I. Tzanakis[3], P. Srirangam[4], W.U. Mirihanage[1,2*],

D.G. Eskin[3], A.J. Bodey[5], and P.D. Lee[1,2]

[1]*Manchester X-ray Imaging Facility, University of Manchester, Manchester M13 9PL, UK*

[2]*Research Complex at Harwell, Didcot OX11 0FA, UK*

[3]*Brunel Centre for Advanced Solidification Technology, Brunel University, London, Uxbridge UB8 3PH, UK*

[4]*WMG, University of Warwick, Coventry, CV4 7AL, UK*

[5]*Diamond Light Source Ltd, Didcot, OX11 0DE, UK*

*Corresponding author

Abstract

Knowledge of the kinetics of gas bubble formation and evolution under cavitation conditions in molten alloys is important for the control casting defects such as porosity and dissolved hydrogen. Using *in situ* synchrotron X-ray radiography, we studied the dynamic behaviour of ultrasonic cavitation gas bubbles in a molten Al-10 wt% Cu alloy. The size distribution, average radius and growth rate of cavitation gas bubbles were quantified under an acoustic intensity of 800 W/cm^2 and a maximum acoustic pressure of 4.5 MPa (45 atm). Bubbles exhibited a log-normal size distribution with an average radius of 15.3 ± 0.5 μm. Under applied sonication conditions the growth rate of bubble radius, $R(t)$, followed a power law with a form of $R(t)=\alpha t^{\beta}$, and $\alpha=0.0021$ & $\beta=0.89$. The observed tendencies were discussed in relation to bubble growth mechanisms of Al alloy melts.

Keywords: Synchrotron X-ray radiography; Ultrasound cavitation; Cavitation bubble; Degassing; Al-Cu alloy

Graphical abstract

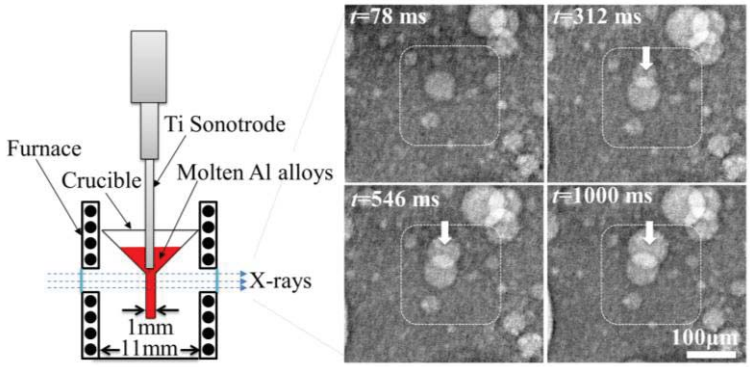

Experimental setup and the dynamics of cavitation gas bubble growth in a liquid Al-Cu alloy

1. Introduction

Liquid metal engineering, including the application of external physical fields, is regarded as an important approach for the control of microstructure and the resulting mechanical properties of many metallic materials [1-3]. Ultrasonic treatment has been employed in solidification processing to achieve structure control [4], grain refinement [5] and degassing [6]. Particularly, its application to light metal (Al and Mg-based) alloys has attracted great interest recently [7]. The mechanisms of ultrasonic treatment include formation, oscillation and collapse of cavitation bubbles; thus promoting melt degassing, wetting and dispersion of solidification phases, including refinement of primary intermetallics and dendrite fragmentation [5-8]. Understanding of ultrasonic cavitation mechanisms and cavitation bubbles through experimental investigation can significantly contribute to reducing casting defects such as porosity through effective control of the dissolved hydrogen content [6]. In addition, such studies can provide insights on other cavitation-related phenomena such as fragmentation and deagglomeration [8-10], and for the validation of numerical models [9, 10].

With conventional characterisation techniques, it has been difficult to directly observe ultrasonic cavitation in molten metals due to their opaqueness and high temperature. In recent years, synchrotron X-ray imaging has been extensively applied to the *in situ* study of solidification [2, 11, 12], fragmentation [8, 13] and coarsening mechanisms [14], pore and bubble growth during solidification [15, 16], and semi-solid processing [17-19]. Huang et al. [20] recently reported measurement of the size distribution of cavitation gas bubbles in an Al-Cu alloy melt using the synchrotron X-ray radiography whilst the current authors used it to study the ultrasonic capillary effect in a molten metallic alloy [21]. Tan et al. [22] observed shockwaves and flows upon cavitation in Bi-based alloys. However, the growth behaviour, number density and underlying mechanisms of cavitation bubble have not been investigated.

In this article we report an *in situ* synchrotron X-ray radiography experiment in which we observed cavitation bubbles induced by an external ultrasound field in a molten Al-10 wt% Cu alloy. Collected statistical data of cavitation bubbles was used to analyse their size distribution and dynamics. The results are discussed in relation to ultrasonic melt degassing.

2. Methods

2.1. Experiments

In situ synchrotron X-ray radiography was conducted at the I13-2 Diamond-Manchester Imaging Branchline of Diamond Light Source, UK. The experimental setup is shown in Fig. 1(a) with key dimensions of the boron nitride (BN) crucible and furnace shown in Fig. 1(b). A bespoke PID-controlled resistance furnace ('Etna') [17] equipped with an X-ray translucent window, was integrated into the beamline to melt and contain the samples. Al-10 wt% Cu alloy samples were pre-machined in order to fit the cavity of the crucible and both were placed at the centre of the furnace cavity.

The crucible was machined from BN due to the material's low X-ray attenuation relative to the Al-Cu alloy. Its cavity was 1.00±0.05 mm wide (in the direction of beam propagation), which provided reasonable imaging capability under the filtered pink beam (mode energy ~15 keV). The alloy was melted and stabilized at 660±10 ^{o}C (~30 °C above the liquidus). Subsequently, a Ti sonotrode with a 1 mm diameter tip, mounted on an ultrasonic processor operating at 30 kHz (Hielscher, Germany), was immersed to a depth of ~4 mm in the melt. The ultrasonic processor was used to generate longitudinal mechanical vibrations by means of electric excitation (reverse piezoelectric effect). A $CdWO_4$ scintillator-coupled pco.edge 5.5 (PCO AG, Germany) camera along with ×8 optical magnification module provided a field of view of 2.1×1.8 mm and an effective pixel size of 0.81 μm. The camera operated at 13 frames per second (fps) with an exposure time of 25 ms. The centre of the viewing window was located ~5 mm below the sonotrode tip. The ultrasonic processing

parameters used in this work are summarized in Table I. As a result, an output pressure of 4.5 MPa is effectively generated on the tip of the sonotrode in the melt, calculated using the analytical model in [23].

Table I. Conditions of external ultrasound field imposed on the alloy melt.

Parameters	Working specification
Driving frequency	30 kHz
Amplitude (peak-to-peak)	28 μm
Pulse-pulse mode factor	50% per second (i.e. one cycle duration: 1 s)
Acoustic power density	800 W/cm^2
Processing time	44 s (i.e. 44 cycles)

2.2. Image analysis

Cavitation bubbles were usually found to be approximately spherical, i.e., circular in 2D radiographs. Some may also be hemispherical or truncated spheres if touching or attached to the crucible. We used an automated technique for multiple-circle detection in 2D radiographs, based on the Circular Hough Transform (CHT) [24] to determine bubble radius. This CHT-based approach employs a Sobel edge detector [25] to highlight sharp changes in intensity and a thinning algorithm [26] to repeatedly remove pixels from the edges of circular objects until they are reduced to single-pixel-wide shapes (i.e. topological skeletonisation). This image processing pipeline was integrated into the ImageJ software package [27].

3. Results and discussion

3.1. Time-resolved radiographs

Figs. 2(a)-(d) show a series of radiographs collected via *in situ* synchrotron radiation X-ray imaging while an Al-10 wt% Cu alloy melt was subjected to an imposed ultrasound

field. Note that Fig. 2 presents a local region from the bottom part of the field of view (~5-6 mm away from the sonotrode tip) where bubbles were minimally disturbed by the cavitation zone in our observation. The gas (bubble interior) and the alloy have very different X-ray attenuation coefficients; this produced good contrast which enabled us to identify bubbles easily. The sonicator pulse sequence is shown in Fig. 2(g). Fig. 2(e) and (f) were generated by subtracting (b) from (a) and (c) from (b), respectively.

Fig. 2(a), (b) and (c) represent the typical appearance of cavitation bubbles in the presence of an ultrasound field during one cycle (1000 ms). Fig. 2(a) shows the cavitation bubbles generated in the ultrasound field shortly after the start of sonication (78 ms). Fig. 2(b) suggests that the ultrasonication enables a steady growth of cavitation bubbles before it stops at 500 ms. When a new cycle starts, existing bubbles disappear and new cavitation bubbles are formed, as shown in Fig. 2(d). It is also apparent that the majority of bubbles grow slightly in size within our observation capacity. For example, the radii of bubbles marked with 'A', 'B' and 'C' in Fig. 2 are increased from 32±1 μm to 44±1 μm, from 81±1 μm to 97±1 μm, and from 101±1 μm to 118±1 μm as the time is progresses from 78 ms to 1000 ms (i.e. the end of the cycle), respectively. This suggests a fast initial growth within a very short time. The growth of bubbles can be observed more clearly by detecting the movements of bubble edges and/or the changes of relative distances between bubbles, since bubbles in this region are less disturbed by the liquid flow induced by the sonotrode. As a qualitative example directly appearing in the images, the edges of the two closely positioned bubbles in the dashed box in Fig. 2(a) overlap (in the 2D radiography images) in its sequential images in Figs. 2(b) & (c), indicating the growth and/or movement of bubbles with time.

By subtracting image (b) from image (a), the bubble evolution under sonicating conditions can be determined. As can be seen from the difference image in Fig. 2(e), i.e. from the crescent shapes on one side of cavitation bubbles (indicated by solid white arrows), the

majority of bubbles increased in size, while the centre of most bubbles shifted slightly downwards. This downward motion is assumed to be caused by pressure wave of the sonication source, which is located above and out of the image.

Interestingly, instead of collapsing/dissolving or floating upwards to the melt surface when sonication is ceased at 500 ms of each cycle, most cavitation bubbles stayed in their positions and continued to grow in size until the end of a cycle at 1000 ms. We thus think that the observed bubbles in these radiographs (Fig. 2a-d) are probably attached to the inner surface of the crucible in most of the time of each cycle, i.e. from 78 ms to 1000 ms in each cycle. As can be seen from the difference image in Fig. 2(f), formed by subtracting frame (c) from frame (b), the white ring-like shapes suggest that cavitation bubbles grew in size relatively more homogeneous as compared to those during the period from 78 ms to 500 ms (their growth indicated in Fig. 2e) and minimal bubble motion was observed during this period of time. Note that the image noise in Fig. 2(e) is much larger than that in Fig. 2(f) due to the presence of the ultrasound field. The growth of bubbles which are attached to the surface of container at this stage (500 ms to 1000 ms) is probably due to the hydrogen diffusion through the crucible wall into the bubbles.

As demonstrated in Fig. 3, we can hypothesize that the following sequence of bubble activities might have happened in a sonication cycle under current sonication conditions (Table I): i) cavitation gas bubbles were generated in cavitation zone just below the sonotrode tip; ii) bubbles then grew rapidly to near the observed size due to the ultrasonication within a very short time (<< 78 ms in this work). In the meantime, these bubbles were transported downwards towards the bottom of the crucible by acoustic streaming/fluid convection, some of which travelled into the cavity of the crucible; iii) bubbles then attached to the inner surface of the crucible or internal oxidation layer between melt and crucible, some of which were located within the field of view where X-rays are passing through the melts. The above

three steps should last no longer than 78 ms after the starting of sonication as the bubbles stabilized within the first radiography of a cycle (see Fig. 2a). After that, bubbles grew in size relatively slow during the period of 78 ms to 500 ms due to the rectified diffusion of dissolved hydrogen into the bubble caused by ultrasonication [7, 28], and continued to grow in size even when the sonotrode was static in a cycle (from 500 ms to 1000 ms), which is hypothesized to be via hydrogen transport through the container. The natural growth of bubbles due to the gas diffusion in the absence of ultrasonic field has also been observed in water [28]. Thus, it seems that under these particular ultrasonication conditions (Table I), cavitation zone was restricted to the region just below the sonotrode tip and the observed cavitation gas bubbles in this work (e.g. those shown in Figs. 2a-d) are probably attached on the surface of container hence not floating up or collapsing/dissolving. The formation of gas bubbles (porosities) on the surface of sample contained in the BN crucible during solidification has also been reported in the literature [29].

Hydrogen is the only known gas with a measureable solubility in molten aluminium or its alloys [30, 31], and when the local pressure is altered or supersaturation conditions are met, gas bubbles can form, mostly on existing substrates in the melt [6, 7, 32], that grow due to the rectified diffusion of dissolved hydrogen into the bubble [6, 7, 28]. When an external force is applied, e.g. via ultrasound, and cavitation conditions are met above the threshold acoustic pressure amplitude, a bubble of a given size will form and grow, while smaller bubbles will tend to dissolve by diffusing gas back into the melt [6, 7, 33] that might be happened for some bubbles (not attached to the crucible surface) above the field of view in this experiment.

3.2. Growth patterns of cavitation gas bubbles

Cavitation is a multi-scale and multi-physics phenomenon [7, 9, 10, 34]. It includes many elementary processes such as bubble nucleation, growth, collapse, travelling/movement,

and so on. In this section, we quantify the size growth of cavitation gas bubbles in the liquid Al-10 wt% Cu alloy under external ultrasound field and investigate the underlying mechanisms of their growth.

It is known that a cavitation bubble can expand its initial size during most of the negative pressure portion of the ultrasound field, approaching a maximum bubble radius, and then contract rapidly and eventually collapse in the succeeding compression phase (the whole time period being a few tens of microseconds [7, 8, 20]). Calculations based on the Minnaert equation [35] for the current processing condition suggest that cavitation gas bubbles in liquid Al can collapse if they reach a critical size (i.e. the resonance size) around 60-70 μm in radius, providing the acoustic pressure is sufficiently high [21, 36]. However, the intensity of the acoustic field may not be sufficient to drive the majority of bubbles to collapse, if i) the position of bubbles is relatively far away from the ultrasonic source and outside the cavitation zone, ii) regular collapses are prevented by the large surface tension (σ), i.e. the pressure inside the bubble (P_g) is higher than that in the liquid (P_l) immediately adjacent to the bubble (Laplace pressure, $P_g - P_l = 2\sigma/R$) [37], and iii) bubbles are stabilized by attaching to the surface of the container.

Fig. 4(a) shows the measured radii of 10 representative bubbles as a function of time (t) within one cycle. Log-log axes are used as it is common while presenting growth behaviour of gas bubbles in liquids [15, 16, 38]. Slightly different growth rates are observed for different gas bubbles that have different initial radii at the time of 78 ms (at which the first radiograph of a cycle was taken). Fig. 4(b) gives the gas bubble growth statistics as a function of time obtained from 130 different measurements. The normalized bubble radius R_{norm} increases with time within each cycle following a power relation: $R_{norm}(t)=\alpha t^{\beta}$, with $\alpha=0.0021$ and $\beta=0.89$ (78 ms < t < 1000 ms). The normalized bubble radius is defined as $R_{norm}=(R-R_{min})/(R_{max}-R_{min})$, where R_{min} and R_{max} are the minimum and maximum radii of bubbles

within each cycle. The regression coefficient R^2=0.94 obtained from the fitting process suggests a reasonable correlation.

According to the literature [8, 20, 39] the typical period of time for a single oscillation of an aluminium cavitation bubble with a maximum radius of ~100 μm is in the order of ~50 μs, predicted using the classical Gilmore model [7, 8, 20, 39]. The captured bubbles in each frame in this work might have already experienced a few hundred oscillations if not imploding since the exposure time used in this work is 25 ms, followed by attaching to the container surface. This cavitation activity could be considered as 'stable cavitation' in terms of lifetime according to Leighton's definition [40], in which case the observed cavitation bubbles exist at relatively low ultrasonic intensities (the acoustic intensity is 800 W/cm^2 at the tip of the transducer but this intensity quickly dissipates inside the cavitation zone and attenuates in the melt [23]), and oscillate for many acoustic cycles with increasing radius before reaching their maximum size followed by their dissolution, implosion or flotation if not touching the container.

It is interesting to note that during first 78 ms of a cycle the radii of bubbles were scattered across a range from ~10 μm to ~100 μm (see Fig. 2a and 4a). This indicates significantly different growth rates of cavitation gas bubbles at their initial stage (t < 78 ms) as compared with later stages (78 ms < t < 1000 ms). This could be due to the inhomogeneity of pressure fluctuation in the liquid melts and the migration of bubbles from the active cavitation zone (just below the sonotrode's tip surface) downwards.

Thus, the average growth in the later stages of gas bubbles (originated from the cavitation zone, travelled downwards and then attached to the container inner surface) is described by a power relation $R_{norm}(t)=0.0021\times t^{0.89}$ (78 ms < t < 1000 ms) under the current ultrasonication conditions (Table I). In contrast, we also observed that some bubbles behaved differently. Fig. 5 exhibits such a case where evolution in time of a single cavitation gas

bubble (bubble '1' shown by white arrows in the dashed boxes) is traced from a series of radiographs (within one sonication cycle, 1.0 s). Fig. 5(a) is taken before the nucleation of this bubble. Fig. 5(b) indicates that the growth process of this bubble has been started and is represented by the light dotted area in the top left region of the existing stable bubble (white arrow) but assumed to be behind/in front in the direction into the page. The bubble rapidly grows until the end of the cycle, with a relatively faster growth rate as compared to the majority of bubbles during most of time of a cycle, as seen in Fig. 5(c) & (d).

We also observed bubble size reduction and even shape change, such as bubble '2' indicated by the red arrows. We think that this is probably due to dissolving of bubble '2' with the release of hydrogen into the melt. The radius of bubble '2' is measured to be ~20±1 μm at 78 ms (see Fig. 4a) and ~14±1 μm (an equivalent radius due to the slightly irregular bubble shape) at the end of cycle (see Fig. 4d). The size of the bubble is much smaller than a calculated value ~65 μm – the resonance size of a hydrogen gas bubble in the liquid Al-10 wt% Cu alloy under current experimental conditions according to the calculation method described in Ref. [35]. It is known that bubbles smaller than the resonance size tend to dissolve into the melt [33], increasing the local hydrogen concentration in the melt and providing additional stimulus (via gas gradient) for the growth of larger cavitation bubbles.

3.3. Size distribution of gas bubbles

Fig. 6(a) shows the statistical size distribution of gas bubbles obtained from 44 radiographs (the first frames of 44 cycles) of X-ray images with full field of view (2.1×1.8 mm). A log-normal distribution of bubble radii is suggested by a fitted curve. It can be seen that the cavitation bubble radius ranges mainly from 10 μm to 80 μm. The inset in Fig. 6(a) shows that cavitation gas bubbles with larger radii (>80 μm) constitute only a few percent in the statistical distribution of number density, but do represent a larger fraction of the bubble volume. The average radius of gas bubbles is 15.3±0.5 μm at the time of 78 ms. In an earlier

work by Huang *et al.* [20], the average size of cavitation bubbles in Al-10 wt% Cu melts was measured to be 30-50 μm. The finer average bubble size in this study is mostly due to the difference in the driving frequency. In ref. [20], a frequency of 20 kHz was used in contrast to the current study where the frequency was 30 kHz. The size of the bubbles is mostly related to the frequency with a higher frequency producing finer bubbles [37, 40].

The bubble number density per unit volume, N_v (mm^{-3}) generated in a specific volume melt was re-calculated from 2D images and shown in Fig. 6(b). Under present ultrasonication conditions (Table I), the possibility of finding 30 bubbles in 1 mm^3 of the liquid Al-10 wt% Cu alloy in each time step of 78 ms is around 32%, while the chance of finding 30-60 bubbles in 1 mm^3 under current conditions is around 80%. These results are significant as they can be used for validation and further improvement of existing numerical models.

4. Conclusions

We used *in situ* synchrotron X-ray radiography to reveal ultrasound cavitation and bubble dynamics in a molten Al-10 wt% Cu alloy. Stable cavitation was observed at a driving frequency of 30 kHz, acoustic intensity of 800 W/cm^2 and a maximum acoustic pressure of 4.5 MPa (45 atm). The majority of bubbles formed and grew rapidly within very short time (<<78 ms) after the start of sonication. Bubbles then travelled downwards by acoustic streaming/fluid convection and some of these bubbles attached on the container surface within the first captured frame (78 ms), followed by a power law growth until the end of each cycle (1000 ms). The average growth is represented by a relation: $R(t)=\alpha t^{\beta}$ with $\alpha=0.0021$ and $\beta=0.89$ (78 ms < t < 1000 ms). The observed bubble kinetics is typical of ultrasonic degassing mechanism which is a process strongly related with rectified diffusion. Statistical considerations show that cavitation gas bubbles exhibit a log-normal size distribution with average radius of 15.3 ± 0.5 μm for this particular experiment. The number density of cavitation bubbles was also quantified for the first time in liquid Al and found that the

possibility of finding 30-60 bubbles in 1 mm^3 alloy melts was around 80% under the applied sonication conditions.

Acknowledgements

The work was made possible by the financial support from the ExoMet Project (which is co-funded by the European Commission in the 7th Framework Programme (contract FP7-NMP3-LA-2012-280421), by the European Space Agency and by the individual partner organisations), from the UK EPSRC grants (EP/I02249X/1, EP/K00588X/1, EP/K005804/1) and the Research Complex at Harwell. The authors wish to acknowledge the use of the Diamond-Manchester Collaboration I13-2 beamline at Diamond Light Source (DLS) (proposal MT9082) and the help provided by colleagues in DLS.

References

[1] H. Men, B. Jiang, Z. Fan, Mechanisms of grain refinement by intensive shearing of AZ91 alloy melt, Acta Mater., 58 (2010) 6526-6534.

[2] E. Liotti, A. Lui, R. Vincent, S. Kumar, Z. Guo, T. Connolley, I.P. Dolbnya, M. Hart, L. Arnberg, R.H. Mathiesen, P.S. Grant, A synchrotron X-ray radiography study of dendrite fragmentation induced by a pulsed electromagnetic field in an A1-15Cu alloy, Acta Mater., 70 (2014) 228-239.

[3] D.G. Eskin, Ultrasonic melt processing: opportunities and misconceptions, Mater. Sci. Forum, 794-796 (2014) 101-106.

[4] A. Das, H.R. Kotadia, Effect of high-intensity ultrasonic irradiation on the modification of solidification microstructure in a Si-rich hypoeutectic Al-Si alloy, Mater. Chem. Phys., 125 (2011) 853-859.

[5] T.V. Atamanenko, D.G. Eskin, L. Zhang, L. Katgerman, Criteria of grain refinement induced by ultrasonic melt treatment of aluminum alloys containing Zr and Ti, Metall. Mater. Trans. A, 41A (2010) 2056-2066.

[6] G.I. Eskin, Cavitation mechanism of ultrasonic melt degassing, Ultrason. Sonochem., 2 (1995) S137-S141.

[7] G.I. Eskin, D.G. Eskin, Ultrasonic treatment of light alloy melts, Second ed., CRC Press, Boca Raton, 2014.

[8] D. Shu, B. Sun, J. Mi, P.S. Grant, A high-speed imaging and modeling study of dendrite fragmentation caused by ultrasonic cavitation, Metall. Mater. Trans. A, 43 (2012) 3755-3766.

[9] G.S.B. Lebon, K. Pericleous, I. Tzanakis, D. Eskin, Application of the "Full Cavitation Model" to the fundamental study of cavitation in liquid metal processing, IOP Conf. Ser-Mat. Sci., 72 (2015) 052050.

[10] L. Nastac, Mathematical modeling of the solidification structure evolution in the presence of ultrasonic stirring, Metall. Mater. Trans. B, 42 (2011) 1297-1305.

[11] M.D. Kang, H.Y. Gao, D. Shu, J. Wang, F.G. Li, Y.A. Fu, L.S.B. Ling, B.D. Sun, In situ and real-time observation of the solidification process of Al-20 mass%Cu alloy by synchrotron X-ray radiography, Mater. Trans., JIM, 55 (2014) 774-778.

[12] R.H. Mathiesen, L. Arnberg, X-ray radiography observations of columnar dendritic growth and constitutional undercooling in an Al-30wt%Cu alloy, Acta Mater., 53 (2005) 947-956.

[13] D. Ruvalcaba, R.H. Mathiesen, D.G. Eskin, L. Arnberg, L. Katgerman, In situ observations of dendritic fragmentation due to local solute-enrichment during directional solidification of an aluminum alloy, Acta Mater., 55 (2007) 4287-4292.

[14] S. Terzi, L. Salvo, M. Suery, A.K. Dahle, E. Boller, Coarsening mechanisms in a dendritic Al–10% Cu alloy, Acta Mater., 58 (2010) 20-30.

[15] P.D. Lee, J.D. Hunt, Hydrogen porosity in directional solidified aluminium-copper alloys: In situ observation, Acta Mater., 45 (1997) 4155-4169.

[16] P.D. Lee, J.D. Hunt, Hydrogen porosity in directionally solidified aluminium-copper alloys: A mathematical model, Acta Mater., 49 (2001) 1383-1398.

[17] B. Cai, S. Karagadde, L. Yuan, T.J. Marrow, T. Connolley, P.D. Lee, In situ synchrotron tomographic quantification of granular and intragranular deformation during semi-solid compression of an equiaxed dendritic Al–Cu alloy, Acta Mater., 76 (2014) 371-380.

[18] K.M. Kareh, P.D. Lee, R.C. Atwood, T. Connolley, C.M. Gourlay, Revealing the micromechanisms behind semi-solid metal deformation with time-resolved X-ray tomography, Nat. Commun., 5 (2014) 4464.

[19] S. Karagadde, P. D. Lee, B. Cai, J. L. Fife, M. A. Azeem, K. M. Kareh, C. Puncreobutr, D. Tsivoulas, T. Connolley, R.C. Atwood, Transgranular liquation cracking of grains in the semi-solid state, Nat. Commun., 6 (2015) 8300.

[20] H.J. Huang, D. Shu, Y.A. Fu, J. Wang, B.D. Sun, Synchrotron radiation X-ray imaging of cavitation bubbles in Al-Cu alloy melt, Ultrason. Sonochem., 21 (2014) 1275-1278.

[21] I. Tzanakis, W.W. Xu, D.G. Eskin, P.D. Lee, N. Kotsovinos, In situ observation and analysis of ultrasonic capillary effect in molten aluminium, Ultrason. Sonochem., 27 (2015) 72-80.

[22] D.Y. Tan, T.L. Lee, J.C. Khong, T. Connolley, K. Fezzaa, J.W. Mi, High-speed synchrotron X-ray imaging studies of the ultrasound shockwave and enhanced flow during metal solidification processes, Metall Mater Trans A, 46A (2015) 2851-2861.

[23] M.M. van Iersel, N.E. Benes, J.T.F. Keurentjes, Importance of acoustic shielding in sonochemistry, Ultrason. Sonochem., 15 (2008) 294-300.

[24] H. Muammar, M. Nixon, Approaches to extending the Hough transform, in: Acoustics, Speech and Signal Processing ICASSP, 1989, pp. 1556-1559.

[25] N. Kanopoulos, N. Vasanthavada, R.L. Baker, Design of an image edge-detection filter using the Sobel operator, IEEE J. Solid-State Circuits, 23 (1988) 358-367.

[26] T.Y. Zhang, C.Y. Suen, A fast parallel algorithm for thinning digital patterns, Commun. ACM, 27 (1984) 236-239.

[27] C.A. Schneider, W.S. Rasband, K.W. Eliceiri, NIH Image to ImageJ: 25 years of image analysis, Nat. Methods, 9 (2012) 671-675.

[28] O.A. Kapustina, Degassing of liquids, in: L.D. Rozenberg (Ed.) Physical principles of ultrasonic technology, Nauka, Moscow, 1970, pp. 253-336.

[29] P.D. Lee, S. Sridhar, Direct observation of the effect of strontium on porosity formation during the solidification of aluminium-silicon alloys, Int. J. Cast Met. Res., 13 (2000) 185-198.

[30] C.E. Ransley, H. Neufeld, The solubility of hydrogen in liquid and solid aluminium, J. Inst. Metals, 74 (1948) 599-620.

[31] D.E.J. Talbot, Effects of hydrogen in aluminium, magnesium, copper, and their alloys, Int. Metall. Rev., 20 (1975) 166-184.

[32] P.D. Lee, A. Chirazi, D. See, Modeling microporosity in aluminum–silicon alloys a review, J. Light Met., 1 (2001) 15-30.

[33] A.R.N. Meidani, M. Hasan, Mathematical and physical modelling of bubble growth due to ultrasound, Appl. Math. Model., 28 (2004) 333-351.

[34] S. Tsuda, S. Takagi, Y. Matsumoto, A study on the growth of cavitation bubble nuclei using large-scale molecular dynamics simulations, Fluid Dyn. Res., 40 (2008) 606-615.

[35] M. Minnaert, On musical air bubbles and the sounds of running water, Philos. Mag., 16 (1933) 235-248.

[36] I. Tzanakis, W.W. Xu, G.S.B. Lebon, D.G. Eskin, K. Pericleous, P.D. Lee, In situ synchrotron radiography and spectrum analysis of transient cavitation bubbles in molten aluminium alloy, Phys. Procedia, 70 (2015) 841-845.

[37] O.V. Abramov, High-intensity ultrasonics : theory and industrial applications, Gordon & Breach, Amsterdam, 1998.

[38] B.B. Mikic, W.M. Rohsenow, P. Griffith, On bubble growth rates, Int. J. Heat Mass Transfer, 13 (1970) 657-666.

[39] F.R. Gilmore, The growth or collapse of a spherical bubble in a viscous compressible liquid, Hydrodynamics Laboratory Report, 26-4 (1952) 1-40.

[40] T.G. Leighton, The acoustic bubble, Academic, London, 1994.

Captions

Fig. 1. (a) *In situ* ultrasonic processing setup on Diamond-Manchester branchline. (b) Schematic diagram of the furnace and crucible (inset is the view along X-ray beam). Main components: I – furnace; II – Ti sonotrode integrated with the ultrasonic processor; III – camera.

Fig. 2. Typical behaviour of cavitation bubbles under present sonication conditions (see Table I): (a) 78 ms after the start of sonication; (b) sonication stops at 500 ms; (c) end of cycle

(1000 ms); (d) 78 ms after the start of a new cycle; (e) image difference by subtracting frame (b) from frame (a); (f) image difference by subtracting frame (c) from frame (b). (g) Schematic pulse model of the sonication corresponding to radiographs from (a)-(d).

Fig. 3. Sketch map of cavitation gas bubble activities under current ultrasonication (Table I): i) bubble generation in cavitation zone (region close to the sonotrode tip); ii) bubble travelling downwards towards the bottom of the crucible; iii) bubble attachment onto the inner surface of the container, some of which are located within the field of view where X-rays are passing through the melts. A number of key dimensions are indicated.

Fig. 4. Cavitation gas bubble growth: (a) radii of cavitation bubbles (R) vs time (t) of 10 representative cases; (b) normalized radii of cavitation gas bubbles (R_{norm}) as a function of t for 130 different measurements. The average growth rate of bubble radii is suggested by a power relation: $R_{\mathrm{norm}}(t)=0.0021\times t^{0.89}$ (78 ms < t < 1000 ms), as indicated by the solid blue line. The ultrasound pulse mode is indexed in (a).

Fig. 5. Nucleation and fast growth of a single cavitation gas bubble: (a) just before nucleation; (b) <78 ms after the nucleation process starts and is represented by the light dotted area on top left region of the bubble's periphery (white arrow); (c) in growth process; (d) the end of growing process at the end of cycle (1.0 s).

Fig. 6. (a) Cavitation bubbles size distribution obtained from the X-ray image series at 78 ms of each cycle. A lognormal size distribution is suggested (blue line). The inset is the enlargement of the tail of the distribution indicated by the dashed box; (b) bubble number density, N_v.

Table I. Conditions of external ultrasound field imposed onto alloy melt.

Figure1
Click here to download high resolution image

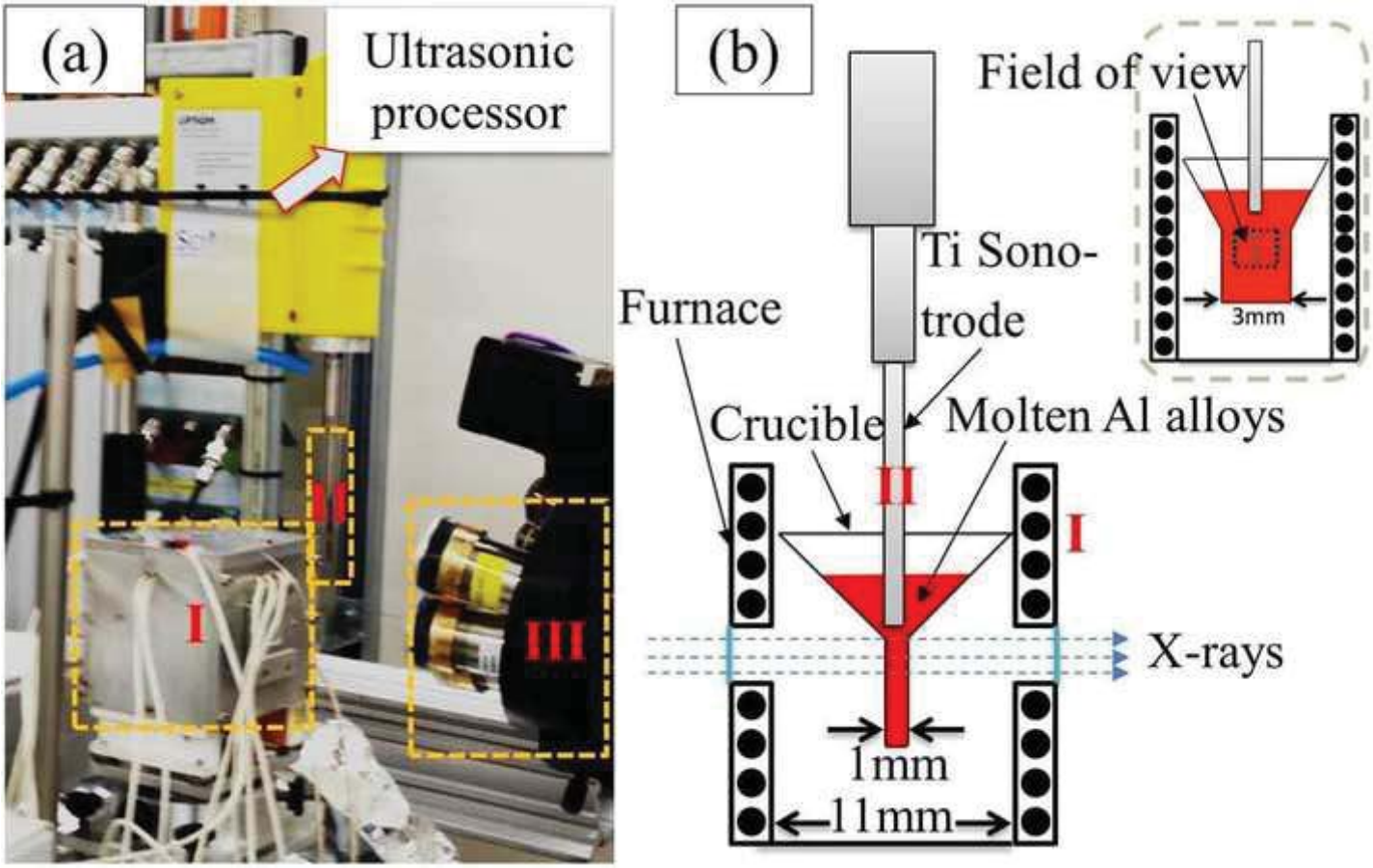

Figure2
Click here to download high resolution image

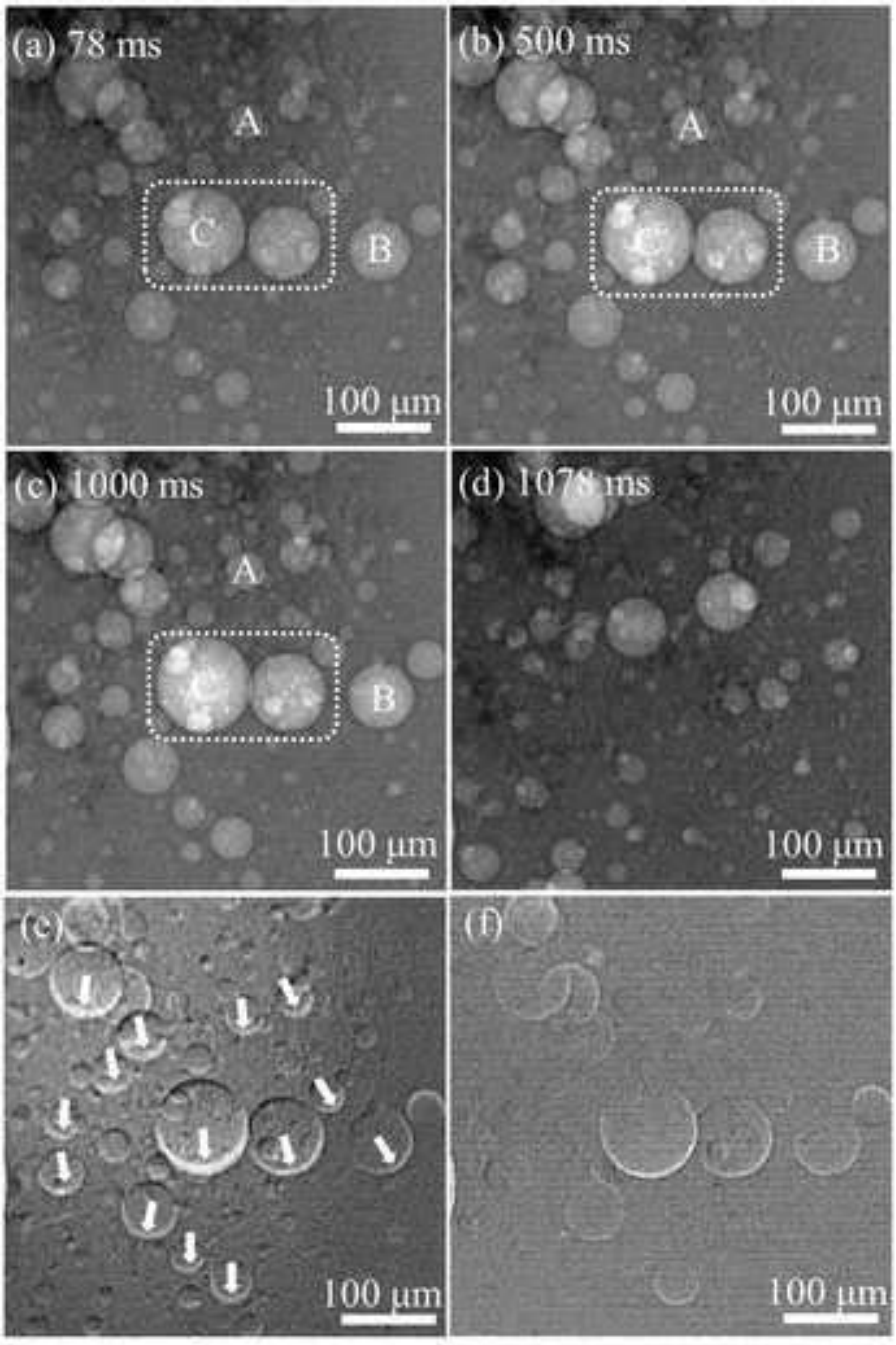

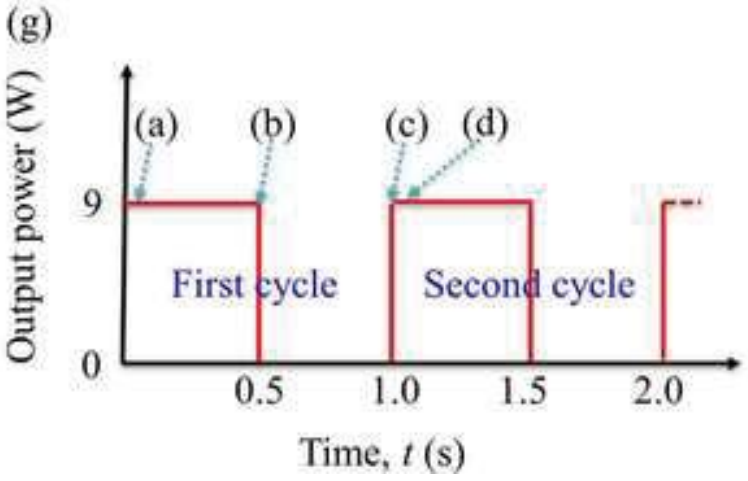

Figure3
Click here to download high resolution image

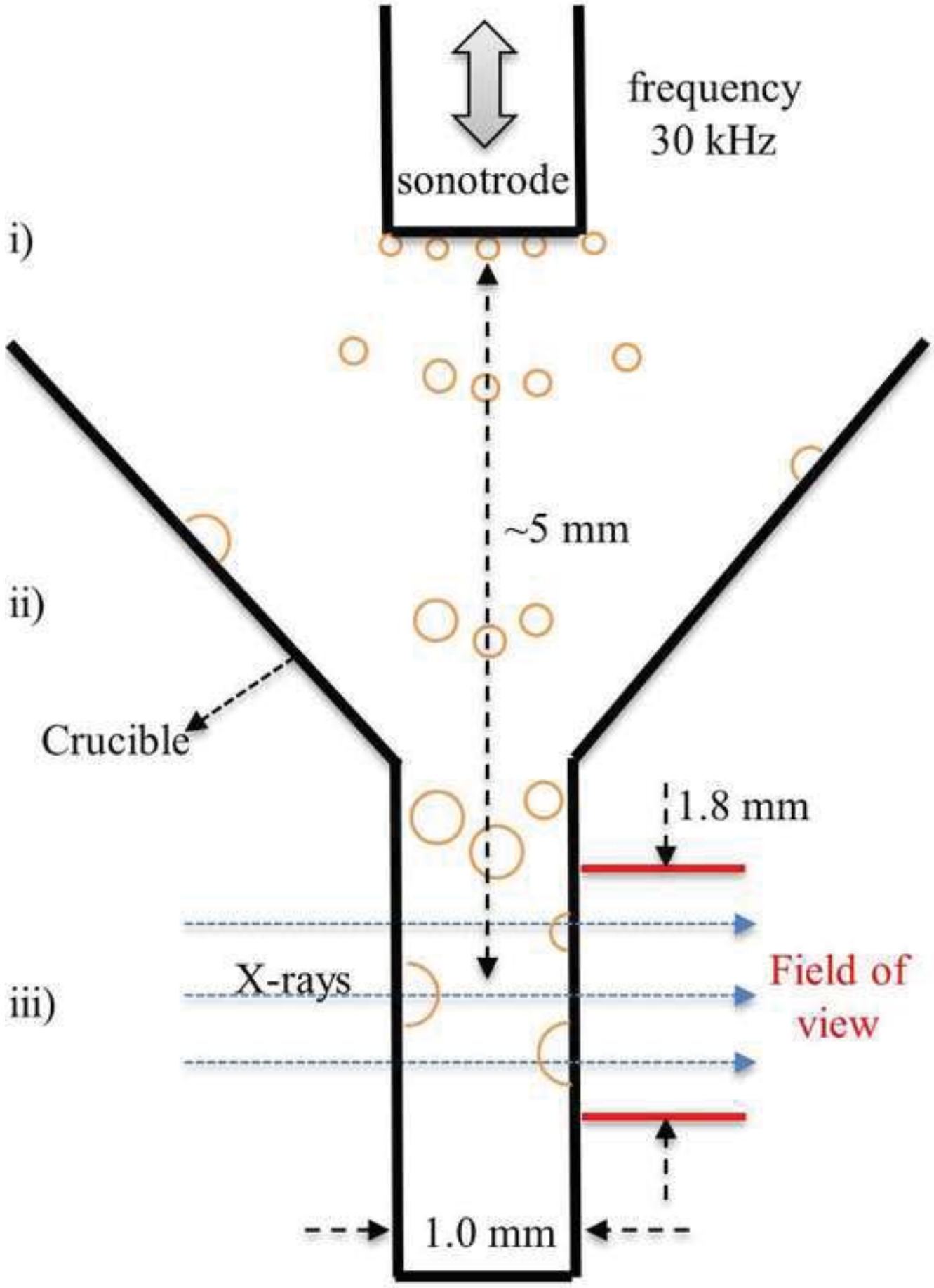

Figure4
Click here to download high resolution image

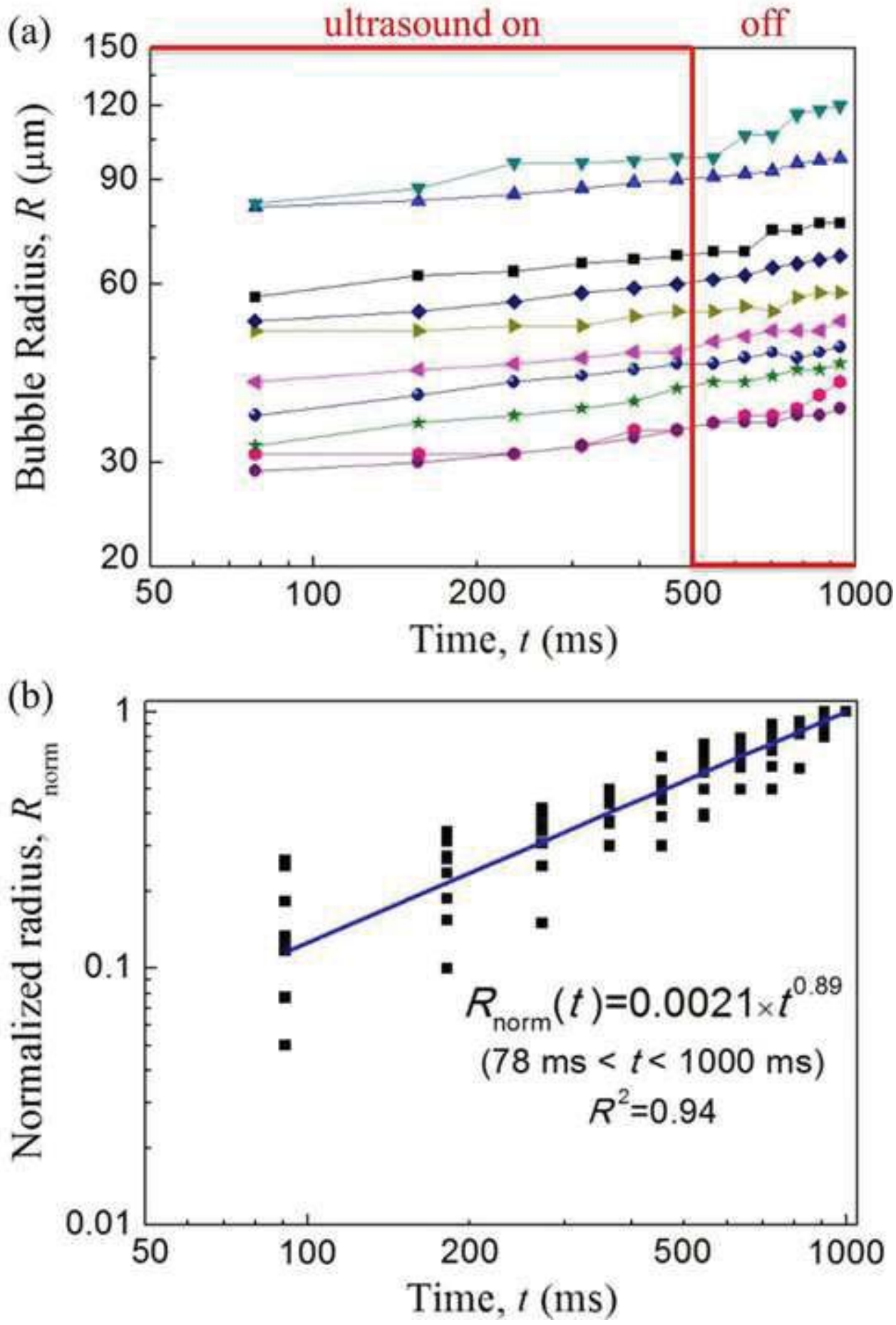

Figure5
Click here to download high resolution image

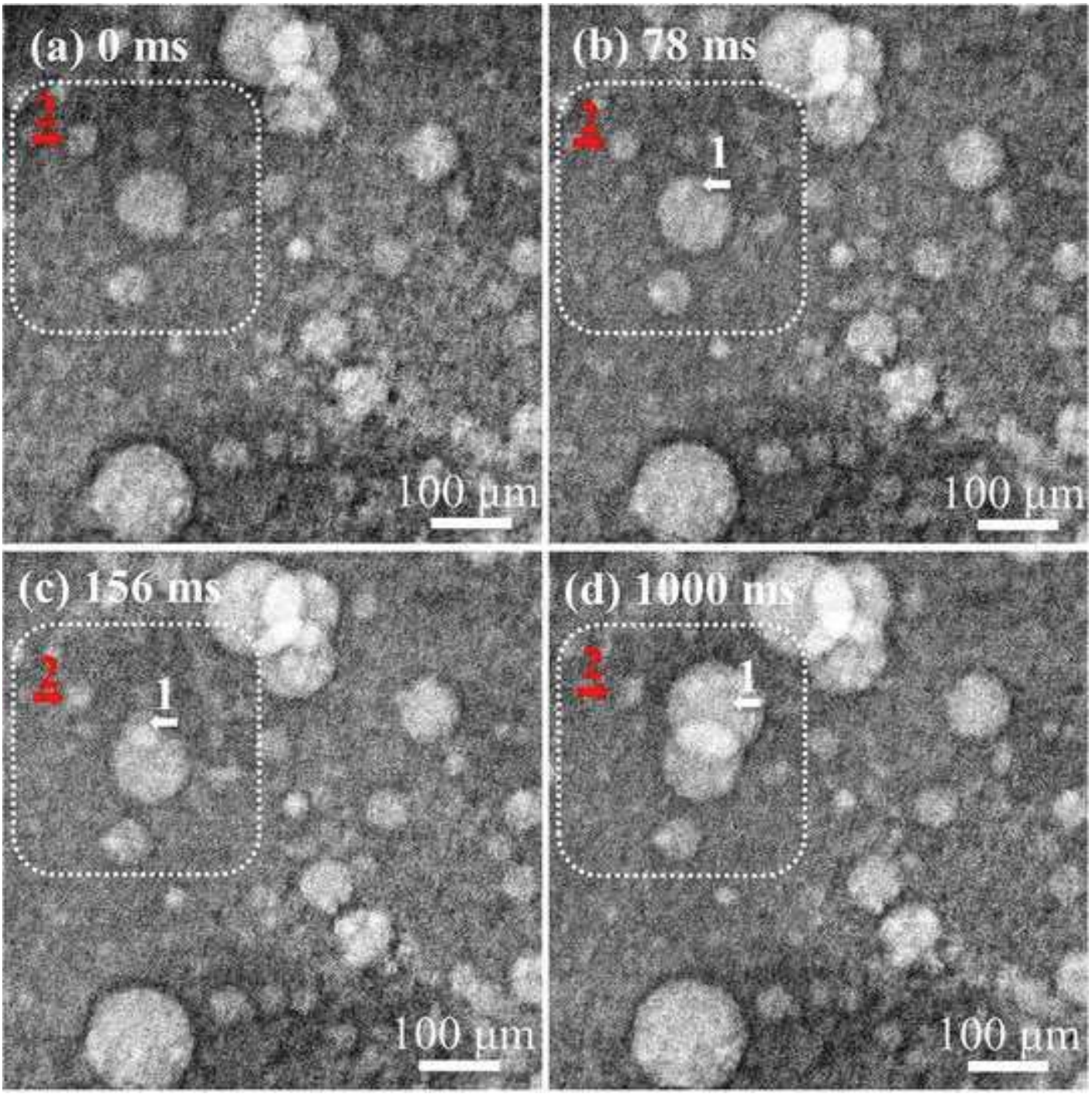

Figure6
Click here to download high resolution image